Available online at www.sciencedirect.com
SCIENCE DIRECT®
International Journal of Mass Spectrometry 241 (2005) 271–282
International Journal of Mass Spectrometry
www.elsevier.com/locate/ijms

Experimental and theoretical studies of charge transfer and hydride transfer in the reactions of OD^+ and C_2H_4

Xiaohui Cai, Yue Li, Elizabeth Richards O'Grady, James M. Farrar*

Department of Chemistry, University of Rochester, Rochester NY 14627, USA

Received 24 November 2004; accepted 8 December 2004
Available online 8 January 2005

Abstract

We present a crossed beam and density functional theory (DFT) study of the dynamics of charge transfer and hydride transfer in collisions of OD^+ with C_2H_4 at relative collision energies between 19.3 and 102 kJ mol^{-1} (0.20–1.06 eV). Charge transfer to form $C_2H_4^+$ is a direct process occurring through large impact parameters. A comparison of the internal energy distributions of reaction products with the photoelectron spectrum of C_2H_4 is consistent with a Franck–Condon picture for long distance electron transfer. Charge transfer with H/D rearrangement to form $C_2H_3D^+ + OH$ does not occur, unlike the related system $D_2O^+ + C_2H_4$, in which comparable amounts of $C_2H_4^+$ and $C_2H_3D^+$ are observed. This difference is accounted for by the significantly smaller proton affinity of OH relative to H_2O. Reactive processes are initiated by the formation of a protonated oxirane triplet diradical, which undergoes intersystem crossing to the singlet manifold. Formation of $C_2H_3^+ + HOD$, nominally a hydride transfer reaction, is shown to occur at the lowest collision energy through transient singlet intermediates in which the timescale for rate-limiting hydrogen atom migration corresponds to a significant fraction of a rotational period. Formation of hydride transfer products is sufficiently exothermic ($\Delta H = -489$ kJ mol^{-1}) that a fraction of the $C_2H_3^+$ products may be formed above the dissociation threshold to $C_2H_2^+$. Increasing collision energy results in enhanced yields of $C_2H_2^+$ relative to $C_2H_3^+$, consistent with unimolecular decay of the most highly excited $C_2H_3^+$ products. However, the very small translational energy releases at all collision energies also require significant vibrational excitation in the HOD products; the most probable internal excitation in HOD is approximately 60 kJ mol^{-1} at all collision energies.

Keywords: Ion–molecule reaction; Potential energy surface; Intersystem crossing; Reaction dynamics; Charge transfer

1. Introduction

Gas phase ion–molecule reactions play an important role in establishing the chemical composition and reactivity patterns in interstellar gas clouds and planetary atmospheres [1,2], electrical discharges [3], combustion processes [4,5], and chemical ionization mass spectrometry [6]. The processes of charge transfer and light particle exchange, including hydride, proton, and hydrogen atom transfer, are among the important prototype reactions implicated in such systems. Light particle transfer between two heavier functional groups is governed both by kinematic and dynamical constraints, and studies in the gas phase may distinguish the roles of these distinct factors. Conventional treatments of exoergic charge transfer reactions often consider the processes as occurring at long range, with little momentum transfer between the approaching reactants or the separating products [7]. Energy resonance and favorable Franck–Condon factors are often cited as playing a key role in electron transfer [8].

In a recent study from our laboratory, we presented a detailed experimental and theoretical study of the charge transfer and proton transfer reactions that occur between ionized water and ethylene molecules [9]. Those data showed that the product internal energy distributions in the charge transfer reaction to form $C_2H_4^+$ were consistent with long range electron transfer governed by favorable Franck–Condon factors

* Corresponding author. Tel.: +1 585 2755834; fax: +1 585 276 0205.
E-mail address: farrar@chem.rochester.edu (J.M. Farrar).

1387-3806/$ – see front matter © 2004 Elsevier B.V. All rights reserved.
doi:10.1016/j.ijms.2004.12.012

for removal of an electron from ethylene. Isotopic labeling studies with D_2O^+ reagents showed that charge transfer with H/D exchange to form $C_2H_3D^+$ products was facile, occurring with a cross section only a factor of two smaller than that for direct charge transfer. Density functional theory (DFT) calculations of important reactive intermediates and the transition states connecting them, in conjunction with statistical Rice–Ramsperger–Kassel–Marcus (RRKM) calculations [10,11], predicted H/D exchange rates more than three orders of magnitude smaller than observed. The DFT calculations also predicted that proton transfer occurs along a coordinate in which the incoming proton approaches the π-cloud of C_2H_4 perpendicular to the C–C bond axis. The experimental data showed a clear progression in the ν_{10} vibration generated by the D atom bridging the carbons in the nascent $C_2H_4D^+$ products, consistent with the DFT prediction.

In the present work, we report a crossed beam and DFT study of the reactions between the hydroxyl cation and ethylene. We employ the isotopically-labelled cation OD^+ instead of OH^+, and focus on the following reactions:

$$OD^+ + C_2H_4 \rightarrow OD + {C_2H_4}^+, \quad \Delta H = -241\,\mathrm{kJ\,mol^{-1}} \tag{1}$$

$$OD^+ + C_2H_4 \rightarrow HOD + {C_2H_3}^+, \quad \Delta H = -489\,\mathrm{kJ\,mol^{-1}} \tag{2}$$

$$OD^+ + C_2H_4 \rightarrow {C_2H_2}^+ + H + HOD, \quad \Delta H = -44.4\,\mathrm{kJ\,mol^{-1}} \tag{3}$$

Reaction (1) appears to be a simple electron transfer to form ${C_2H_4}^+$, while reaction (2) is nominally a hydride abstraction process [12], but may proceed through one or more covalently bound intermediates. Reaction (2) is sufficiently exothermic that the most highly internally excited ${C_2H_3}^+$ products may undergo C–H bond cleavage; the latter process may be thought of either as unimolecular decay via reaction (3), or as a direct collision-induced dissociation process. Experimental data allow this distinction to be made.

The reaction of $OD^+ + C_2H_4$ has been studied previously by Fishman and Grabowski [13]. They used a selected ion flow tube (SIFT) to determine thermal energy rate coefficients and product branching ratios for the ion–molecule reactions of hydroxyl cation, ionized water, and their deuterated analogues with ethylene. In addition to observing ${C_2H_4}^+$ and ${C_2H_3}^+$, these workers also reported rate coefficients for the formation of a product of mass 29, and suggested pathways that could form either the ethyl cation, ${C_2H_5}^+$, or the formyl cation, HCO^+. No firm conclusion was offered concerning the identity of the mass 29 product.

In the present experiments, we report differential cross sections for reactions (1)–(3) over the collision energy range from 19.3 to 102 kJ mol^{-1} (0.20–1.06 eV). Although we observed a very weak signal at mass 29 at the highest collision energy, we were unable to measure a full differential cross section for this channel. In conjunction with DFT calculations, the data provide a clear physical basis for understanding the dynamics of the charge transfer reaction, including an interpretation of energy partitioning and the absence of H/D exchange in this process. In addition, the formation of ${C_2H_3}^+$ is shown to occur via hydrogen atom migrations in reactive intermediates that evolve during the course of the reaction.

2. Experimental

The crossed beam instrument has been described in detail previously [14], so only a brief overview is given here. OD^+ ions are produced by electron impact on deuterium oxide vapor in an ion source held at a pressure of approximately 0.01 torr. Following extraction, the ions are accelerated to 300 eV, and are then mass-selected by a 60° magnetic sector. After deceleration to the desired beam energy and focusing by a series of ion optics, the beam has a roughly triangular kinetic energy distribution with a FWHM between 19 and 43 kJ mol^{-1} (0.20 and 0.45 eV) in the laboratory frame of reference.

Experiments were performed at selected energies over a relative collision energy range of 19.3–102 kJ mol^{-1}. Ethylene beams are formed by supersonic expansion of the pure gas through a 0.07 mm nozzle. A 1.0-mm diameter skimmer located 50 nozzle diameters in distance downstream from the nozzle selects the cool core of the beam. The beam is collimated by passing through a 3.0-mm square aperture located approximately 2.5 cm from the skimmer before entering the main chamber, where it intersects the ion beam at a 90° angle. An electrostatic energy analyzer with resolution of 0.07 eV determines the kinetic energies of ions in the primary ion beam and scattered ionic reaction products. The energy analyzer is calibrated before and after the experiments by measuring the kinetic energy distribution of thermal ions formed by resonant charge transfer between He^+ and He. The energy-analyzed product ions are mass-analyzed by a quadrupole mass filter, and are detected with two microchannel plates in the chevron configuration. High vacuum is maintained in all chambers by oil diffusion pumps. Data acquisition is computer-controlled.

Three independent measurements were performed in the experiment. At each collision energy, the kinetic energy distributions of the scattered product ions were measured at 22 fixed laboratory angles. Each energy spectrum consisted of 80 points, with typical energy bin widths of 0.025 eV. These kinetic energy distributions were then normalized to the angular distributions of product ions at each angle in the laboratory coordinate system. The branching fractions for reactions (1)–(3) were also measured at each collision energy.

3. Data analysis

Dynamical information about a chemical reaction is most easily extracted from the measured kinetic energy and angular distributions of scattered ionic products when viewed in the center of mass (c.m.) frame of reference. The ion and neutral beams contain atoms or molecules with distributions of velocities and the beams have finite spatial widths, resulting in a distribution of collision energies and intersection angles. The spread in reagent beam velocities and intersection angles must be removed from the laboratory data before they are transformed to the c.m. frame to extract the differential cross section for the reaction. An iterative deconvolution procedure based on the method of Siska is used to remove the spread in beam velocities and extract the center of mass cross section $I_{\text{c.m.}}(u, \theta)$ from the laboratory cross section $I_{\text{lab}}(v, \Theta)$ by inverting the following transformation relationship [15]:

$$I_{\text{lab}}(v, \Theta) = \sum_{i=1}^{N} f_i \frac{v^2}{u_i^2} I_{\text{c.m.}}(u_i, \theta_i). \quad (4)$$

In the above equation, v and u_i are the velocities in the laboratory and c.m. coordinates, respectively; the summation is evaluated over a grid of 125 Newton diagrams, corresponding to five energies in each of the two reagent beams, and five intersection angles distributed around 90°; f_i is a weighing factor, or the probability of observing Newton diagram i based on distributions of reagent beam velocity and intersection angle. The extracted $I_{\text{c.m.}}(u, \theta)$ can be transformed back to the lab frame of reference, allowing comparison with the experimental data. When averaged over experimental velocity distributions and beam intersection angles, the c.m. cross sections recover the experimental data with a standard deviation of ≤15%.

The barycentric angular distribution $g(\theta)$ of the ionic product of each reaction is also calculated by averaging the flux distribution over recoil speed, indicated by the bracket notation:

$$\langle g(\theta) \rangle_u = \int_0^{\infty} \mathrm{d}u \; I_{\text{c.m.}}(u, \theta). \quad (5)$$

Similarly, the angle-averaged relative translational energy distribution of products, $P(E'_{\text{T}})$ is given by:

$$\langle P(E'_{\text{T}}) \rangle_\theta = \int_0^{\pi} \mathrm{d}\theta \sin\theta \, u^{-1} \, I_{\text{c.m.}}(u, \theta). \quad (6)$$

The full flux distributions in velocity space as well as the kinetic energy and angular distributions derived from them provide important physical insight into the nature of reactive collisions.

4. Results

4.1. Direct charge transfer: $OD^+ + C_2H_4 \rightarrow OD + C_2H_4^+$

The charge transfer reaction was studied at c.m. collision energies of 19.3, 61, and 102 kJ mol^{-1} (0.20, 0.63, and 1.06 eV). Fig. 1 shows the flux distribution for $C_2H_4^+$ products at 19.3 kJ mol^{-1}, obtained by iterative deconvolution of the lab data and transformation to c.m. coordinates, represented as a contour projection superimposed on the Newton kinematic diagram; the distributions are qualitatively similar at the higher collision energies and are not shown here. In the c.m. coordinate system, the directions of the OD^+ ion beam and the C_2H_4 neutral beam are 0 and 180°, respectively.

The experimental results shown in the flux map indicate that the charge transfer flux distribution is sharply asymmetric, with the majority of the $C_2H_4^+$ products scattered in the same direction as the precursor beam. Because of the convention that the parent ion beam defines the 0° direction in c.m. coordinates, the charge transfer products are assigned to the angular range near 180°. We adopt the convention that such products are forward-scattered since their momenta are similar in direction and magnitude to their precursor neutral reactants.

The angular distributions and relative translational energy distributions of the products of the charge transfer reaction at all three energies are shown in Fig. 2. Angular distributions are sharply forward-scattered, their widths decreasing with increasing collision energy as expected for a direct process governed by long range electron transfer with minimal momentum transfer to the nuclei. The relative translational energy distributions of the product at the three energies are shown in the lower panel of Fig. 2. As the collision energy

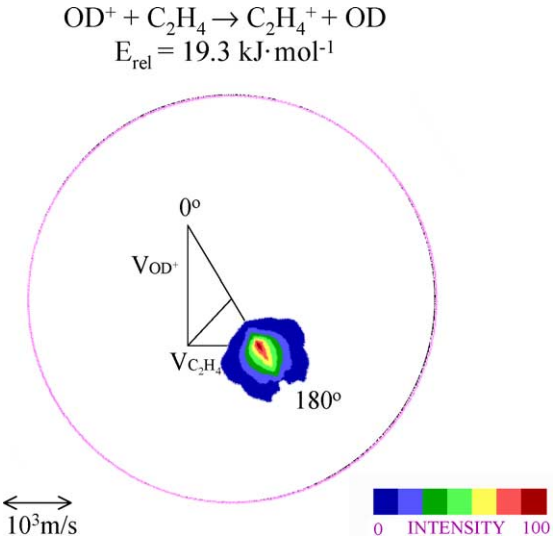

Fig. 1. Contour plot representation of $C_2H_4^+$ product flux at 19.3 kJ mol^{-1} collision energy superimposed on Newton diagram. Circle on contour map defines maximum $C_2H_4^+$ product velocity allowed by energy conservation.

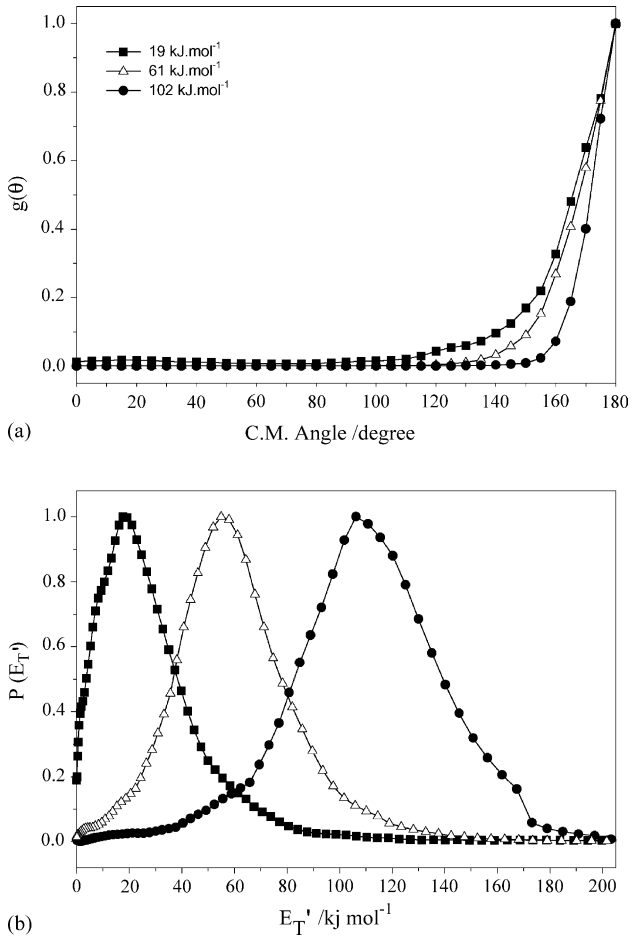

Fig. 2. (a) Angular distributions for $C_2H_4^+$ charge transfer products, all energies. (b) Kinetic energy distributions for $C_2H_4^+$ charge transfer products, all energies.

increases, both the mean energy and the width of the translational energy distribution increases.

The energy disposal results for the charge transfer process to form $C_2H_4^+$ are summarized in Table 1. The total energy is the sum of collision energy E_{rel}, any reactant internal energy, and the reaction exothermicity. The product relative energy E'_T at each collision energy is tabulated as the average value

Table 1
Reaction energy partitioning results for $OD^+ + C_2H_4 \rightarrow OD + C_2H_4^+$ (units in kJ mol^{-1})

Ion energy	23.1 (0.24 eV)	93 (0.96 eV)	160 (1.66 eV)
Reactant relative energy (E_{rel})	19.3	61	102
Total energy (E_{total})	260	302	343
Product average relative energy ($\langle E'_T \rangle$)	32	61	114
$\langle E'_T \rangle / E_{total}$ (%)	12	20	33
Product average internal energy	228	241	229

of the appropriate relative translational energy distribution in the lower panel of Fig. 2. Table 1 shows that the average internal excitation of the reaction products ranges from 229 to 241 kJ mol^{-1}, lying within 5% of the reaction exothermicity of 241 kJ mol^{-1} at all collision energies. Thus, the internal energy distributions of the charge transfer products are essentially independent of collision energy in the range of these experiments.

4.2. *Hydride transfer: $OD^+ + C_2H_4 \rightarrow HOD + C_2H_3^+$*

The formation of products of mass 27 is formally a hydride transfer from C_2H_4 to OD^+, although this term does not necessarily imply that the process occurs by direct particle abstraction. Fig. 3 shows the c.m. flux distribution for $C_2H_3^+$ products at the lowest collision energy of 19.3 kJ mol^{-1}. Although the dominant feature in the flux distribution is a peak near the ethylene beam corresponding to forward-scattered products, a careful analysis shows that there is also a weak component in the backward direction. Close inspection of the flux distribution in Fig. 3 shows that the most probable speeds of the forward and backward components of the distribution are quite similar. That conclusion is reinforced by decomposing the angular-averaged recoil distribution of Eq. (6) into two terms. By setting the limits of integration in Eq. (6) to (0, π/2) or (π/2, π), the recoil distributions for backward or forward scattered products, respectively, can be evaluated separately. The results of those calculations, shown in Fig. 4, demonstrate clearly that the recoil distributions are effectively independent of scattering angle, a hallmark of a transient complex that lives a significant fraction of a rotational period. This is an important point, in that it significantly reduces the probability that the bimodal flux distribution is

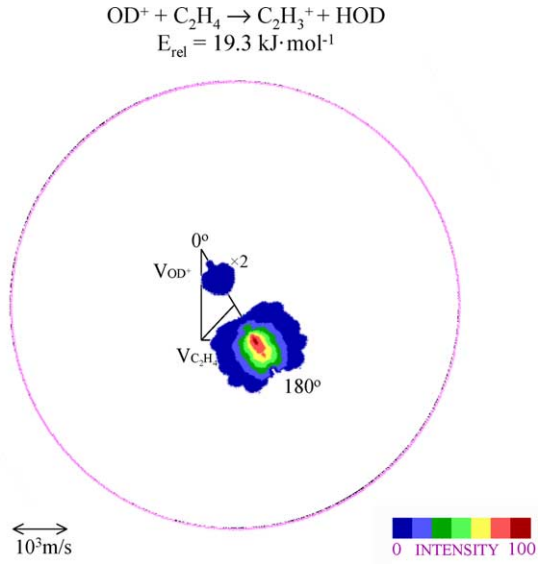

Fig. 3. Contour plot representation of $C_2H_3^+$ product flux at collision energy of 19.3 kJ mol^{-1} superimposed on Newton diagram, lowest collision energy. Circle on contour map defines maximum $C_2H_3D^+$ product velocity allowed by energy conservation.

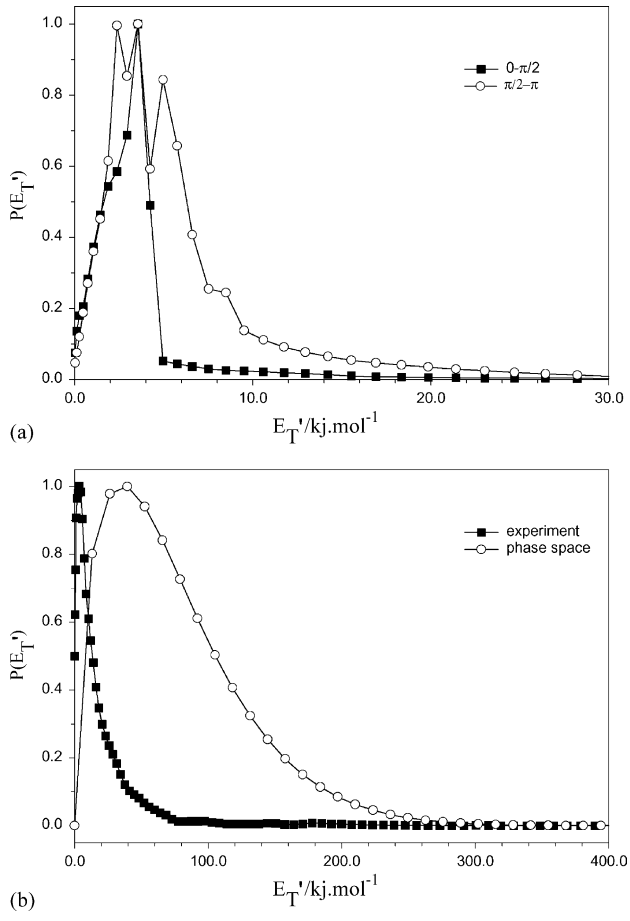

Fig. 4. Upper panel: kinetic energy distributions for $C_2H_3^+$ hydride transfer products at 19.3 kJ mol^{-1}. Forward and backward scattering distributions are shown separately. Lower panel: phase space calculation as discussed in the text.

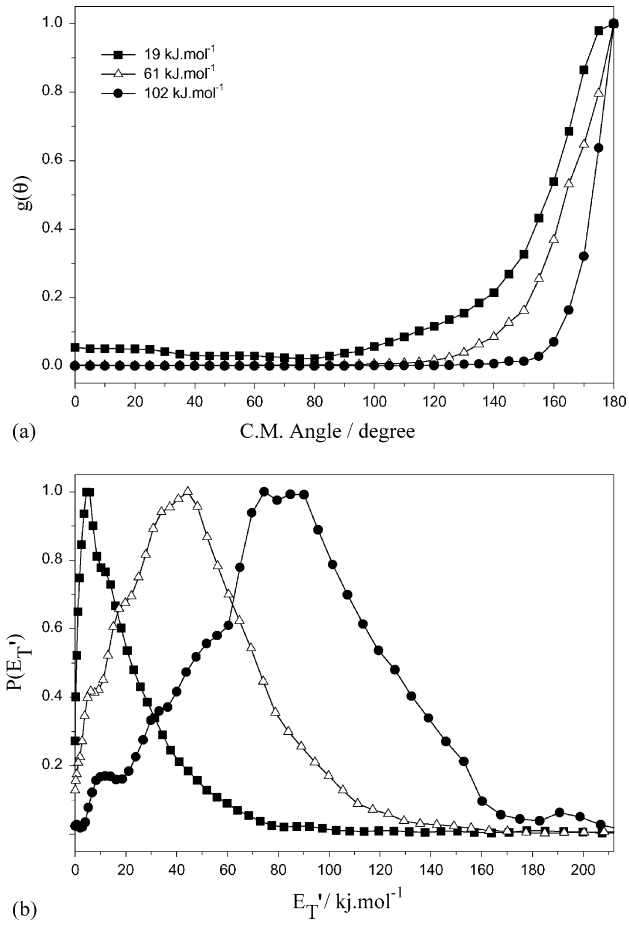

Fig. 5. (a) Angular distributions for $C_2H_3^+$ hydride transfer products, all energies. (b) Kinetic energy distributions for $C_2H_3^+$ hydride transfer products, all energies.

a superposition of two mechanisms, one producing forward scattering, the other resulting in backward scattering. Also shown in Fig. 4 is the result of a model statistical calculation of the product kinetic energy distribution, which will be discussed in the next section.

In Fig. 5, we show the angular and kinetic energy distributions for $C_2H_3^+$ products at all three collision energies. The upper panel shows the angular distributions averaged over product velocity. Consistent with the flux map of Fig. 3, the angular distribution at the lowest collision energy shows a weak but perceptible component of backward scattering. This component of backward scattering is absent at higher collision energies. As will be noted later, the magnitude of this component relative to the stronger forward-scattered peak provides information on the decay lifetime of the complex. The lower panel of Fig. 5 show the angular-averaged kinetic energy distributions of the $C_2H_3^+$ products at all three collision energies. All of the distributions show evidence for incompletely resolved structure to the low energy side of the maxima, especially near 10 kJ mol^{-1}. This structure may arise from populating specific vibrational modes of the products, but the large numbers of vibrational modes preclude their assignment in this system. Numerical results are summarized in Table 2.

Although the precise nature of energy partitioning among the $C_2H_3^+$ and HOD products cannot be determined unambiguously from the data shown in Fig. 5, energy conservation does require important constraints on the partitioning of the energy. At the lowest collision energy, the total energy accessible to reaction products is 508 kJ mol^{-1}, whereas

Table 2
Reaction energy partitioning results for $OD^+ + C_2H_4 \rightarrow HOD + C_2H_3^+$ (units in kJ mol^{-1})

Ion energy	23.1 (0.24 eV)	93 (0.96 eV)	160 (1.66 eV)
Reactant relative energy (E_{rel})	19.3	61	102
Total energy (E_{total})	508	550	591
Product average relative energy ($\langle E'_T \rangle$)	28	52	93
$\langle E'_T \rangle / E_{total}$ (%)	5.5	9.5	16
Product average internal energy	480	498	498

the dissociation thresholds for C–H bond cleavage in the $C_2H_3^+$ products, or for O–H(D) bond cleavage in HOD, are 445 and 499 kJ mol^{-1}, respectively. Thus, reaction products formed at a relative collision energy of 19.3 kJ mol^{-1} with less than ~63 kJ mol^{-1} of translational energy may have sufficient energy to dissociate to $C_2H_2^+ + H + HOD$; products with translational energy less than 9 kJ mol^{-1} may dissociate to $C_2H_3^+ + H(D) + OD(H)$. Similarly, at collision energies of 61 and 102 kJ mol^{-1}, products formed with translational energies below 105 and 147 kJ mol^{-1}, respectively may have internal excitation in excess of the dissociation threshold to $C_2H_3^+$. The corresponding limits for HOD dissociation are 51 and 93 kJ mol^{-1}, respectively. Statistical partitioning of energy in the $C_2H_3^+ + HOD$ products places the majority of the available energy in $C_2H_3^+$; in conjunction with the significantly lower dissociation threshold in $C_2H_3^+$ relative to HOD, we expect $C_2H_2^+$ to be the major decay fragment of the nascent products formed by hydride transfer. Fig. 5 shows that the translational energy distributions of $C_2H_3^+$ products at all three collision energies fall almost entirely in the range where enough energy is available for dissociation of $C_2H_3^+$. As discussed later, the lifetimes of all decaying species are significantly shorter than the transit time through the detection system, resulting in negligible kinetic shifts. Thus, the mechanism for formation of reaction products at such low translational energies requires that the HOD products contain sufficient internal excitation to be formed in concert with stable $C_2H_3^+$ products. At the peaks of the translational energy distributions shown in Fig. 5, the magnitudes of HOD internal excitation all lie within ±10% of 60 kJ mol^{-1}. This observation suggests that dynamical constraints place a fixed amount of product internal excitation in HOD, and that the $C_2H_3^+$ products populate internal energy states up to the dissociation limit. The low energy downturn in the translational energy distributions in Fig. 5 corresponds to the onset of dissociation, subject to the constraint that HOD products have approximately 60 kJ mol^{-1} of internal excitation. In the next section, we report on direct observation of the products of dissociation.

4.3. Unimolecular decay of excited $C_2H_3^+$ products

At each collision energy, products were detected at mass 26, corresponding to the formation of $C_2H_2^+$. A close examination of the experimental data allows us to demonstrate that $C_2H_2^+$ is formed by unimolecular decay of highly excited $C_2H_3^+$. Similar observations of $C_2H_2^+$ formed by unimolecular decay of $C_2H_3^+$ have been reported in the literature [16]. In Fig. 6, we plot the $C_2H_2^+$ flux distribution at 19.3 kJ mol^{-1} relative to the center of mass of the original reactants. Measurement of the flux distribution of a single product from a collisional process forming three fragments is kinematically indeterminate. However, careful inspection of the experimental data and close comparison with the flux distributions for the parent $C_2H_3^+$ products allow a number of robust conclusions to be made.

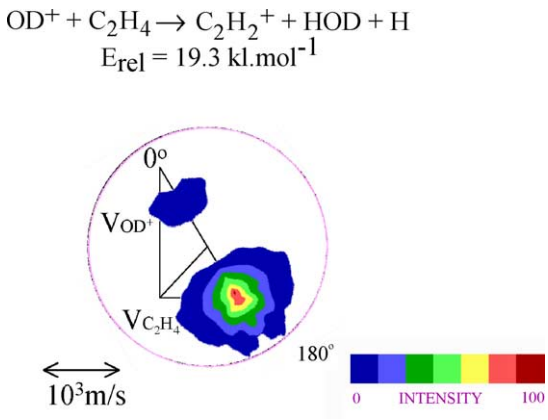

Fig. 6. Contour plot representation of $C_2H_2^+$ product flux at collision energy of 19.3 kl mol^{-1} superimposed on Newton diagram.

The first salient characteristic of the $C_2H_2^+$ distribution is that it bears a remarkable resemblance to the corresponding $C_2H_3^+$ flux distribution. If the $C_2H_2^+$ products arise from hydrogen atom ejection from decaying $C_2H_3^+$ products, the kinematics of dissociation require that the momenta of the ejected H and $C_2H_2^+$ fragments be equal and opposite in the reference frame of the decaying parent. The c.m. speed of the nascent $C_2H_2^+$ can only be 1/27 of the relative velocity of the separating fragments. Thus, we expect the distributions of daughter $C_2H_2^+$ products in velocity space to originate from the parent $C_2H_3^+$ flux distributions. The fact that the $C_2H_2^+$ flux distribution is broadened only slightly relative to the parent $C_2H_3^+$ distribution implies that only a small fraction of the 64 kJ mol^{-1} excess energy appears in product translation, as statistical theories of unimolecular decay would predict. The kinematic simplification arising from light particle ejection allows this analysis to be placed on a more quantitative basis and will appear in a separate publication from this laboratory.

The second clear conclusion coming from the experimental data of Fig. 6 concerns the appearance of both forward and backward scattered peaks. The backward scattered peak, whose existence in the $C_2H_3^+$ distribution shown in Fig. 3 was considered strong evidence for the participation of long-lived transient intermediates, is even stronger relative to the forward peak in the $C_2H_2^+$ flux distribution. As described in the previous paragraph, $C_2H_2^+$ products are formed in regions of velocity space in the immediate vicinity of their $C_2H_3^+$ precursors. The fact that the backward peak is more intense in the fragments than in the parents suggests that a majority of the $C_2H_3^+$ products have decayed to $C_2H_2^+$, at least for parents in this region of velocity space.

4.4. Product branching ratios

Careful measurements of the intensities of the products of reactions (1)–(3) were obtained at all three collision energies. Independent of collision energy, the charge transfer process corresponds to 75% of the total reactive flux, in reasonable agreement with the value of 66% reported at thermal energy

by Fishman and Grabowski [13]. The remainder of the reactive flux arises from hydride transfer, both in the form of nascent $C_2H_3^+$ and its unimolecular decay daughter $C_2H_2^+$. The observed ratio for $C_2H_3^+$ to $C_2H_2^+$ products is unity at the lowest collision energy of 19.3 kJ mol^{-1} and decreases smoothly to approximately 0.4 at the highest collision energy of 102 kJ mol^{-1}. This result is also consistent with the formation of $C_2H_2^+$ by unimolecular decay of $C_2H_3^+$.

4.5. DFT calculations

In order to gain insight into different intermediates and reaction pathways that may be accessible to the $OD^+ + C_2H_4$ collision system, we have carried out DFT calculations with the Gaussian 98 program package [17]. The calculations focus on the structures of intermediates of singlet multiplicity having nominal stoichiometry $[OH{\cdot}C_2H_4]^+$ and probe pathways for the formation of ground state $C_2H_4^+$ and $C_2H_3^+$ products. The key issues that we attempt to understand are the following: the absence of a charge transfer process coincident with H/D rearrangement, unlike the results of previously reported work from our lab with D_2O^+ reactants [9], and the formation of $C_2H_3^+$ products via a complex that appears to survive a significant fraction of a rotational period at low collision energies. Fishman and Grabowski [13] proposed a series of reaction pathways that bear a resemblance to the results discussed here.

The OH^+ reagent has a triplet ground state. In a manner analogous to the isoelectronic $O(^3P) + C_2H_4$ system [18], we expect the approaching OH^+ to undergo electrophilic addition to the π-bond of ethylene to form a triplet diradical corresponding to ring-opened protonated oxirane. As characterized by Yamaguchi et al. [19], the p-type diradical orbitals are orthogonal in this oxirane system, leading to favorable matrix elements for spin–orbit coupling and subsequent rapid intersystem crossing to the singlet manifold [20]. Our DFT calculations show that this triplet species lies ∼300 kJ mol^{-1} below the reactants.

The geometrical parameters of all relevant species on the lowest singlet surface were fully optimized at the HF/6-31G(d) and DFT(UB3LYP)/6-31+G(d,p) levels. The transition states were calculated using the synchronous transit-guided quasi-Newton (STQN) method [21,22]. The stationary points and the first-order saddle points were confirmed through the calculation of harmonic vibrational frequencies. The frequencies of the deuterated species were calculated with proper substitution of hydrogen by deuterium. These frequency results are used in the RRKM calculations discussed later. The transition states were assigned through the frequency analysis. In order to obtain more reliable energetics, the single point energy calculations were performed at the DFT(UB3LYP)/6-311++G(d,p) level on the basis of the B3LYP/6-31+G(d,p) equilibrium geometries. In this study, the expectation values of the total square of the spin angular momentum, $\langle S^2 \rangle$, are very close to 0.75 for all doublet state species. For triplet state OH^+, $\langle S^2 \rangle$ is equal to 2.01. Thus, spin contamination may be ignored. The geometrical parameters, and energy and frequency results obtained in this study are listed in the supporting information of this paper.

Fig. 7 shows the schematic energy diagram of reactants, products, and key intermediates important in the reaction dynamics of $OH^+ + C_2H_4$. The DFT calculations, obtained at the B3LYP/6-311++G(d,p) level with zero-point vibrational energy corrections, focus on singlet intermediates and the products formed from them. All energies are calculated relative to the energy of the approaching reactants. The diagram also shows the energy of the triplet protonated oxirane diradical calculated by DFT, as well as electrostatic complexes

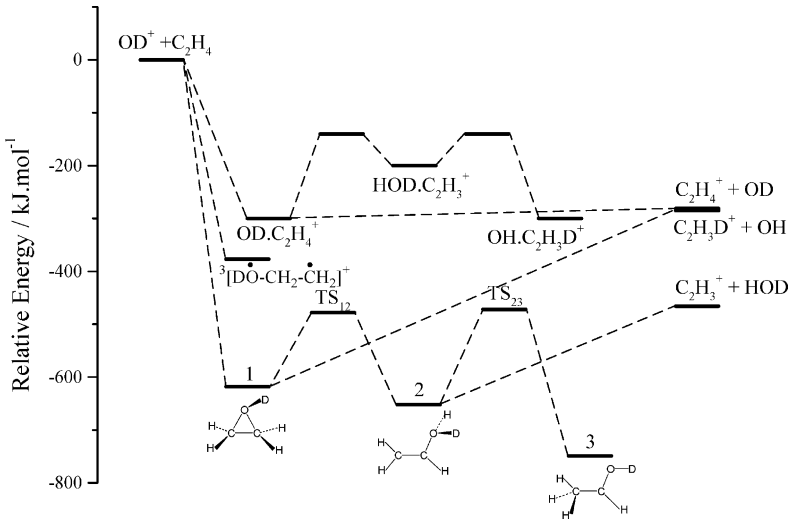

Fig. 7. Schematic reaction coordinate for the $OD^+ + C_2H_4$ system. As discussed in the text, charge transfer occurs through the $OD{\cdot}C_2H_4^+$ electrostatic complex. Intersystem crossing of triplet protonated oxirane to the singlet manifold precedes hydride transfer and unimolecular decay. Properties of all complexes and transition states are discussed in the text and in the Supplementary data.

implicated in the charge transfer process, as described later.

The first $[OH{\cdot}C_2H_4]^+$ isomer characterized, denoted intermediate **1** in Fig. 7, is protonated ethylene oxide, in which two carbon atoms and oxygen form a three-membered ring with the hydrogen atom of the hydroxyl group pointed out of the C–C–O plane. This is precisely the structure that one would expect from ring closure of the nascent singlet protonated oxirane species formed upon intersystem crossing. The calculations show that this species is bound by 618 kJ mol^{-1} relative to the reactants, compared to a value of 643 kJ mol^{-1} evaluated from tabulated thermodynamic data. A second intermediate, denoted **2**, lies 33 kJ mol^{-1} below **1**, and is formed by cleavage of the C(1)–O bond to open the three-membered ring, followed by a hydrogen atom shift from C(2) onto the oxygen atom. In isomer **2**, the three heavy atoms are in a plane and H(7) and H(8), the hydrogens bound to oxygen, lie nearly symmetrically on opposite sides of the C_s symmetry plane. Intermediate **2** may undergo C–O bond cleavage to form the $C_2H_3^+$ product.

A third structure, denoted **3**, lies 131 kJ mol^{-1} below **1** and corresponds to protonated acetaldehyde, which is precisely the expected product from ring opening of protonated ethylene oxide. Our calculations showed that **3** evolves from complex **2**, rather than along a direct path from **1**. The calculation also shows that **3** does not lead to the observed $C_2H_3^+$ products, but should undergo C–C bond cleavage to form $CH_3 + HCOH^+$. The latter product, the protonated formyl radical, was not observed in our experiments. Another isomer, denoted **4**, is structurally similar to **3**, differing only in the orientation of the OH bond relative to the C–C framework. Like **3**, this species does not correlate with observed products. Finally, an isomer of $[C_2H_4{-}OH]^+$, denoted **5**, in which a hydronium ion orients a single hydrogen atom toward the π-electron system of an incipient C_2H_2 molecule was also found, but was considered unimportant because the expected H_3O^+ (or H_2DO^+) decay products were not observed.

In an early theoretical study on the 2-hydroxyethyl cation system, Hopkinson et al. [23] obtained structure **1** at the HF/4-31G level. They also obtained an open chain structure, $[H_2CCH_2{-}OH]^+$. Our calculations also obtained the same structure at the HF/4-31G level, but further optimization at the HF/6-31G(d) and UB3LYP/6-31+G(d,p) level of theory shows that this structure has an imaginary frequency associated with the torsional motion of the CH_2 group to which O is bonded, and is therefore a transition state associated with hydrogen atom migration, denoted **6**. Fig. 7 omits structures **4**, **5**, and **6**, but their properties are reported in the Supplementary data.

5. Discussion

The DFT calculations provide a natural focus for a discussion of the reaction dynamics in the $OD^+ + C_2H_4$ system. Fig. 7 shows the initial triplet diradical protonated oxirane species, which undergoes rapid intersystem crossing to the singlet manifold. The singlet diradical closes to form protonated ethylene oxide, **1**. Isomerization of **1** to the ring-opened structure **2** occurs through **TS12**, a transition state with an energy of 140 kJ mol^{-1} relative to complex **1**, only 12 kJ mol^{-1} lower than the energy of the $C_2H_3^+ + HOD$ products, which form directly from **2**. Finally, intermediate **3**, corresponding to protonated acetaldehyde, which our calculations show is accessible through intermediate **2**, lies only ∼130 kJ mol^{-1} below **1**. The transition state **TS23** for this isomerization lies 180 kJ mol^{-1} above **2**.

The reaction coordinate for $C_2H_3^+$ formation is a classic double minimum system [24,25] in which the rate-determining step is passage through **TS12** associated with ring opening and hydrogen atom migration. The DFT calculations of the structures of complexes **1** and **2** and the transition states connecting them with each other and with the reaction products allow statistical rate constants to be calculated via RRKM theory. We expect that rates below ∼10^{13} s^{-1} are consistent with the assumption of rapid intramolecular vibrational relaxation prior to dissociation, whereas calculated rates significantly larger than this value provide qualitative confirmation that the processes are direct. At a collision energy of 19.3 kJ mol^{-1}, the total non-fixed energies of complex **1** and the critical configuration at **TS12** are 638 and 498 kJ mol^{-1}, respectively. Using vibrational frequencies obtained from the DFT calculations, we find that the rate constant for the **1** → **2** isomerization process is 8×10^{12} s^{-1}. The entropy of activation for the isomerization process is +9.9 J K^{-1} mol^{-1}. In like manner, the rate constant for decomposition of complex **2** by C–O bond cleavage to form $C_2H_3^+$ and HOD products at the same collision energy is 1.2×10^{15} s^{-1}, more than two orders of magnitude faster. The entropy of activation for this process is +59.5 J K^{-1} mol^{-1}, confirming the "loose" nature of the transition state for this simple bond cleavage process. Thus, the formation of $C_2H_3^+$ products does not occur by direct hydride abstraction, but proceeds via complex **1**, followed by ring opening and hydrogen atom migration to form complex **2**, with subsequent C–O bond cleavage.

The interconversion rate for **2** → **3** via **TS23** is calculated via RRKM theory to be 2.5×10^{11} s^{-1}, nearly four orders of magnitude slower than direct decay of **2** to $C_2H_3^+$. The entropy of activation for this reaction is calculated to be −12.7 J K^{-1} mol^{-1}, indicative of a tight transition state. Thus, formation of protonated acetaldehyde is not expected to be an important pathway in this system, consistent with the absence of any products that correlate with this intermediate.

The geometry of the incipient HOD bond in complex **2** provides some insight into the mechanism for forming vibrationally excited HOD molecules upon cleavage of the C–O bond. The DFT calculations show that the HOD bond angle in the complex is approximately 111°, appreciably greater than the equilibrium value of 104.5° in the free molecule. Relaxation of the H–O–D bond angle to its equilibrium value may impart significant bending excitation to the nascent product.

One quantum of HOD bending is approximately 17 kJ mol^{-1}, so only a relatively small number of quanta are required to impart a mean internal excitation of 60 kJ mol^{-1} to this product. More detailed studies of this issue are required to provide further insight into this dynamical constraint.

The angular distribution asymmetry observed both in the parent $C_2H_3^+$ and daughter $C_2H_2^+$ flux distributions at low energy provides experimental confirmation that the process is not direct, but is mediated by one or more transient intermediates. The "osculating model" for chemical reactions [26–28] proceeding through complexes that live a fraction of a rotational period parameterizes the forward–backward asymmetry in the angular distribution in terms of the ratio of the complex lifetime to its rotational period. According to the model, the asymmetry is written as:

$$g(\pi)/g(0) = \cosh(\tau_R/2\tau) \quad (7)$$

where τ is the complex lifetime and τ_R its rotational period. The low energy angular distribution shown in Fig. 5 suggests that $g(\pi)/g(0) \approx 10$ and thus $\tau_R/\tau \approx 6$. The DFT calculations allow the rotational constants of complexes **1** and **2** to be evaluated (~8 GHz). Rate constant data [13] provide an estimate of the maximum impact parameter for complex formation, leading to a value of 160 $\hbar$ for the total angular momentum of the complex. Under these conditions, the rotational period is estimated to be 700 fs, resulting in a lifetime of ~110–120 fs. This result is in fortuitously good agreement with the RRKM lifetime inferred from the rate of isomerization through **TS12**, 8×10^{12} s^{-1}. From the perspective of rate limiting isomerization, the formation of hydride transfer products is in reasonable accord with statistical theory at the lowest collision energy.

The kinetic energy distributions for $C_2H_3^+$ formation at the lowest collision energy give an additional perspective on the statistical character of the reaction. Unlike rate measurements, which only probe the transition state region, kinetic energy distributions provide information on the transition state as well as energy transfer processes that occur as the products leave the transition state. Seminal work by Hase and co-workers [29–32] has helped clarify the relationship between rate and kinetic energy measurements and the modification of the distribution of energy at the transition state by exit channel interactions and angular momentum constraints. The statistical phase space theory (PST) of unimolecular decay as introduced by Light et al. [33] and elaborated by Bowers and Chesnavich [34] calculates the kinetic energy distribution by counting all microstates of the products accessible from a complex of constant total energy and angular momentum as equally probable.

In Fig. 4, we show the results of PST for the product kinetic energy distribution from a complex with total angular momentum of 160 $\hbar$. In comparison with the experimental results, the calculated kinetic energy distribution is shifted to higher energies and is significantly broader than observed experimentally. Thus, the internal energy distribution is significantly "hotter" than statistical. Although many reported examples of experimental kinetic energy distributions are broader than PST distributions and are ascribed to incomplete randomization of the total energy, experimental distributions that are "hotter" than statistical are more unusual. A classic example of such behavior has been reported by Graul and collaborators [35,36] on the S_N2 nucleophilic substitution reaction of $Cl^- + CH_3Br$, in which the nascent C–Cl bond retains high levels of internal excitation. Hase and coworkers [37–40] have provided a theoretical rationalization of this behavior through calculations showing that a significant fraction of reactive collisions avoid the entrance channel well and react in a direct fashion with dynamical specificity. As we have already noted, the formation of $C_2H_3^+$ products requires that they be formed in concert with HOD products with a constant amount of vibrational excitation. The possibility that non-statistical kinetic energy distributions in the present case arise from the dynamical constraints that form such products must be considered.

The DFT calculations also provide a basis for establishing the pathway for charge transfer. In intermediate **1**, the charge is localized on the carbons; as a result, simple cleavage of two C–O bonds leads directly to $OD + C_2H_4^+$ products. Although we were unable to characterize the transition state leading to charge transfer products from **1**, we can estimate the upper limit for this rate via a loose, orbiting transition state; the RRKM rate for this process is 1.2×10^{13} s^{-1}. If complex **1** serves as the common intermediate for charge transfer and hydride transfer, then one would predict that the upper bound on the branching ratio for charge transfer is 60%, in fair agreement with the experimentally determined value of 75%. However, a decay rate of this magnitude would produce an angular distribution for charge transfer with backward scattering of intensity comparable to that observed for $C_2H_3^+$ formation. The absence of such backward scattering peaks in the charge transfer data argues against a pathway involving covalently bound intermediates such as **1**. If the proper transition state for charge transfer is "tight" and is therefore rate limiting, then the observed branching ratio for charge transfer from **1** should be smaller and the backward scattering contribution to the angular distribution should be larger, both of which contradict experiment.

The large cross sections and strongly forward peaked angular distributions observed for exoergic charge transfer are consistent with the occurrence of electron transfer at length scales characteristic of electrostatically rather than covalently bound intermediates. In analogy with the related $D_2O^+ + C_2H_4$ system [9], we examine the possible role of a pathway for charge transfer that involves an electrostatically bound $[OD{\cdot}C_2H_4]^+$ complex formed by the long-range attraction of approaching reagents. We were unable to characterize such electrostatic complexes by DFT in the presence of the strongly bound covalent intermediates discussed above, but the DFT results for electrostatically bound intermediates in the closely-related $[D_2O{\cdot}C_2H_4]^+$ system provide significant guidance. In that system, the nearly 200 kJ mol^{-1}

difference in ionization potentials between D_2O and C_2H_4 causes the first electrostatically bound intermediate to be $D_2O{\cdot}C_2H_4^+$, in which the electron has already been transferred from C_2H_4 to D_2O^+. The ionization potential of OD is 0.40 eV (38.6 kJ mol^{-1}) larger than that of D_2O, suggesting that a similar situation holds and that the electrostatic complex formed when OD^+ approaches C_2H_4 also has the positive charge on the latter species. The $OD{\cdot}C_2H_4^+$ complex lies no more than 300 kJ mol^{-1} below the reagents, as contrasted with the covalent complexes **1** and **2**, which are bound in excess of 600 kJ mol^{-1}. As described in detail in our previous publication, the RRKM decay rate of such an electrostatic complex to the charge transfer products should be of magnitude 10^{14} s^{-1}, a full order of magnitude faster than decay of the more strongly bound covalent complex to the products of charge transfer.

Finally, we must account for the absence of H/D exchange leading to $OH + C_2H_3D^+$. Along the covalent pathway, a sequence of isomerizations in which ring-opening and migration of a hydrogen atom bound to carbon convert **1** to **2**, followed by the reverse of this process, but with migration of the oxygen-bound deuterium to carbon, i.e., a $\mathbf{2} \rightarrow \mathbf{1}'$ process, would produce a precursor to $C_2H_3D^+$. The RRKM rate for the $\mathbf{2} \rightarrow \mathbf{1}'$ process is 3×10^{11} s^{-1}, approximately 3% of the rate for direct decay of 1 to $C_2H_4^+$. However, this latter process must compete with dissociation of **2** to $C_2H_3^+$, proceeding with a rate estimated to be $\sim 10^{15}$ s^{-1}. Less than one complex **2** in 1000 will lead to charge transfer with H/D exchange, for an effective H/D exchange rate $\leq 3 \times 10^8$ s^{-1}. Although the H/D exchange rate along the covalent pathway is below our detection limits, consistent with experimental data, the observed angular distributions for charge transfer are inconsistent with this pathway, requiring us to reject it.

The issue of H/D exchange along the electrostatic complex pathway requires us to consider the following sequence of H^+ and D^+ exchanges:

$$OD \cdot C_2H_4^+ \rightleftharpoons HOD^+ \cdot C_2H_3 \rightleftharpoons HO \cdot C_2H_3D^+ \qquad (8)$$

The lower bound on the barrier to the first proton transfer should be approximately equal to the difference in the proton affinities of OH (593 kJ mol^{-1}) and C_2H_3 (755 kJ mol^{-1}), or ~160 kJ mol^{-1}. At the lowest collision energy of these experiments, in which the non-fixed energies of the complex and the critical configuration are 320 and 160 kJ mol^{-1}, respectively, the RRKM rate for this intramolecular proton transfer process should be on the order of 10^8 s^{-1}, also below detection limits. The suppression of H/D exchange in the $OD{\cdot}C_2H_4^+$ electrostatic complex by barriers driven by the low proton affinity of OH therefore provides a convincing explanation for the absence of charge transfer with H/D exchange to form $C_2H_3D^+$ products. In addition, the rate of charge transfer along the electrostatic pathway is $\sim 10^{14}$ s^{-1}, consistent with the sharply forward-scattered product angular distributions.

The experimental data for the system $OD^+ + C_2H_4$ suggest that the reaction products are formed through distinct pathways. Access to the different regions of the potential energy surface that result in charge transfer or hydride transfer is controlled by impact parameter. At large impact parameters, the centrifugal barrier effectively prevents trajectories from accessing regions of the surface at short range where significant covalent interactions occur. In contrast, the reactive channels in which chemical bonds are cleaved or formed proceed through interactions in which covalently-bound intermediate complexes live a substantial fraction of a rotational period. Small impact parameter collisions provide access to the characteristic length scales where such intermediates may form.

The charge transfer process appears to proceed as a direct reaction, occurring at large impact parameters, with long distance electron transfer, such that the momenta of the products are changed minimally from that of the precursor reactants. The internal energy distributions of the reaction products may be extracted by energy conservation from the measured translational energy distributions of Fig. 3 as follows:

$$P_{\text{int}}(E'_{\text{T}}) = P_{\text{trans}}(E_{\text{total}} - E'_{\text{T}}). \qquad (9)$$

Experimental work on the photoelectron spectrum of the product C_2H_4 provides useful information on the nature of the Franck–Condon envelope for formation of $C_2H_4^+$ [41], and provides a useful comparison with the present experimental data. This comparison is shown in Fig. 8. First, we notice that internal energy distributions of products at all three collision energies are very similar and cut off at the thermochemical limit. Second, the photoelectron band for production of $C_2H_4^+$ in the 1^2B_{2g} excited state is energy resonant and also has large Franck–Condon factors. The similarity of the product internal energy distributions and the

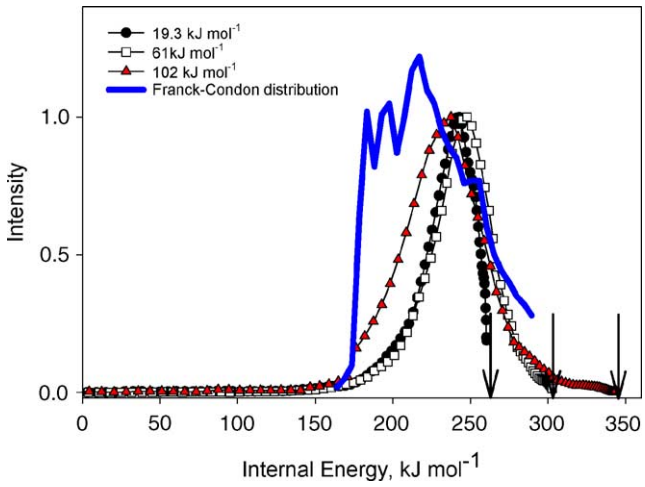

Fig. 8. Internal energy distributions of reaction products for the $C_2H_4^+$ products inferred from product translational energy distributions. The vertical arrows indicate the thermochemical limits for the three different collision energies. The solid curve shows the photoelectron band for formation of $C_2H_4^+$ in the first excited 1^2B_{2g} state.

Franck–Condon profile for ionization of C_2H_4 indicates that the collisional ionization process is very similar to photoionization. As the collision energy increases, the high-energy cut off of the product internal energy distribution, dictated by energy conservation, follows the Franck–Condon profile.

6. Conclusions

As revealed by crossed beam experiments and DFT calculations, both electrostatically and covalent bound intermediates play significant roles in the reactions of OD^+ with C_2H_4. Large impact parameter collisions sample the long-range attractive potential where the electrostatic complex $OD{\cdot}C_2H_4{}^+$ governs the charge transfer reaction. The internal energy distributions of reaction products are consistent with favorable Franck–Condon factors for ionization of C_2H_4. The small proton affinity of OH suppresses the rates of H/D exchange in this complex, leading to the absence of charge transfer products in which H/D scrambling has occurred. This observation contrasts with the related $D_2O^+ + C_2H_4$ system in which such rearrangement is facile.

Low impact parameter collisions allow the reagents to reach intermolecular distances where covalently bound intermediates are formed. The initial intermediate formed is expected to be a protonated oxirane triplet diradical that undergoes rapid intersystem crossing to the singlet manifold. The formation of $C_2H_3{}^+ + HOD$ products appears to proceed through a cyclic intermediate in which ring opening and hydrogen atom migration precede C–O bond cleavage to the final products. At the lowest collision energy, the rate-limiting step corresponds to a complex lifetime of 120 fs, consistent with the asymmetric angular distribution of reaction products. Both the HOD and $C_2H_3{}^+$ products retain significant internal excitation, with at least 50% of the nascent ionic products undergoing dissociation to $C_2H_2{}^+$.

The $OD^+ + C_2H_4$ system has provided an example of the synergy between crossed beam experiments and DFT calculations. We look forward to studies of additional systems of increasing complexity in which such experimental and theoretical methods provide deep insight into the dynamics of molecular collisions.

Acknowledgements

The authors acknowledge their appreciation to the U.S. Department of Energy for its support of this work. We are also grateful to Professor J.P. Dinnocenzo for helpful discussions.

Appendix A. Supplementary data

Supplementary data associated with this article can be found, in the online version, at doi:10.1016/j.ijms.2004.12.012.

References

[1] D. Smith, Chem. Rev. 92 (1992) 1473.
[2] D. Smith, P. Spanel, Mass Spectrom. Rev. 14 (1995) 255.
[3] B. Chapman, Glow Discharge Processes: Sputtering and Plasma Etching, Wiley-Interscience, New York, 1980.
[4] D.J. Hucknall, Chemistry of Hydrocarbon Combustion, Chapman and Hall, London, 1985.
[5] S.D. Tanner, J.M. Goodings, D.K. Bohme, Can. J. Chem. 59 (1981) 1760.
[6] A.G. Harrison, Chemical Ionization Mass Spectrometry, second ed., CRC Press, 1992.
[7] P.M. Hierl, V. Pacak, Z. Herman, J. Chem. Phys. 67 (1977) 2678.
[8] M.T. Bowers, D.D. Elleman, Chem. Phys. Lett. 16 (1972) 486.
[9] L. Liu, X. Cai, Y. Li, E.R. O'Grady, J.M. Farrar, J. Chem. Phys. 121 (2004) 3495.
[10] R.A. Marcus, J. Chem. Phys. 20 (1952) 359.
[11] T. Baer, W.L. Hase, Unimolecular Reaction Dynamics: Theory and Experiments, Oxford University Press, New York, 1996.
[12] O. Dutuit, H. Palm, D. Berthomieu, Z. Herman, Chem. Phys. 209 (1996) 259.
[13] V.N. Fishman, J.J. Grabowski, J. Phys. Chem. A 103 (1999) 4879.
[14] D.F. Varley, D.J. Levandier, J.M. Farrar, J. Chem. Phys. 96 (1992) 8806.
[15] P.E. Siska, J. Chem. Phys. 59 (1973) 6052.
[16] A.B. Rakshit, P. Warneck, Int. J. Mass Spectrom. Ion Phys. 35 (1980) 23.
[17] M.J. Frisch, G.W. Trucks, H.B. Schlegel, G.E. Scuseria, M.A. Robb, J.R. Cheeseman, V.G. Zakrzewski, J.J.A. Montgomery, R.E. Stratmann, J.C. Burant, S. Dapprich, J.M. Millam, A.D. Daniels, K.N. Kudin, M.C. Strain, O. Farkas, J. Tomasi, V. Barone, M. Cossi, R. Cammi, B. Mennucci, C. Pomelli, C. Adamo, S. Clifford, J. Ochterski, G.A. Petersson, P.Y. Ayala, Q. Cui, K. Morokuma, P. Salvador, J.J. Dannenberg, D.K. Malick, A.D. Rabuck, K. Raghavachari, J.B. Foresman, J. Cioslowski, J.V. Ortiz, A.G. Baboul, B.B. Stefanov, G. Liu, A. Liashenko, P. Piskorz, I. Komaromi, R. Gomperts, R.L. Martin, D.J. Fox, T. Keith, M.A. Al-Laham, C.Y. Peng, A. Nanayakkara, M. Challacombe, P.M.W. Gill, B. Johnson, W. Chen, M.W. Wong, J.L. Andres, C. Gonzalez, M. Head-Gordon, E.S. Replogle, J.A. Pople, Gaussian 98; Revision A.11.1; Gaussian, Inc.: Pittsburgh, PA, 2001.
[18] M. Dupuis, J.J. Wendolowski, T. Takada, W.A. Lester Jr., J. Chem. Phys. 76 (1982) 481.
[19] K. Yamaguchi, S. Yabushita, T. Fueno, S. Kato, K. Morokuma, Chem. Phys. Lett. 80 (1980) 27.
[20] L. Salem, C. Rowland, Angew. Chem. Int. Ed. 11 (1972) 92.
[21] C. Peng, H.B. Schlegel, Isr. J. Chem. 33 (1994) 449.
[22] C. Peng, P. Ayala, H.B. Schlegel, M.J. Frisch, J. Comput. Chem. 17 (1996) 49.
[23] A.C. Hopkinson, M.H. Lien, I.G. Csizmadia, K. Yates, Theor. Chim. Acta 47 (1978) 97.
[24] M.J. Pellerite, J.I. Brauman, J. Am. Chem. Soc. 102 (1980) 5993.
[25] M.J. Pellerite, J.I. Brauman, J. Am. Chem. Soc. 105 (1983) 2672.
[26] M.K. Bullitt, C.H. Fisher, J.L. Kinsey, J. Chem. Phys. 60 (1974) 478.
[27] S. Stolte, A.E. Proctor, R.B. Bernstein, J. Chem. Phys. 65 (1976) 4990.
[28] W.R. Creasy, J.M. Farrar, J. Chem. Phys. 87 (1987) 5280.
[29] W.L. Hase, Chem. Phys. Lett. 67 (1979) 263.
[30] E.E. Aubanel, D.M. Wardlaw, L. Zhu, W.L. Hase, Int. Rev. Phys. Chem. 10 (1991) 249.
[31] K. Bolton, W.L. Hase, H.B. Schlegel, K. Song, Chem. Phys. Lett. 288 (1998) 621.
[32] K. Bolton, H.B. Schlegel, W.L. Hase, K.Y. Song, PCCP Phys. Chem. Chem. Phys. 1 (1999) 999.
[33] P. Pechukas, J.C. Light, C. Rankin, J. Chem. Phys. 44 (1966) 794.

[34] W.J. Chesnavich, M.T. Bowers, J. Chem. Phys. 66 (1977) 2306.
[35] S.T. Graul, M.T. Bowers, J. Am. Chem. Soc. 116 (1994) 3875.
[36] S.T. Graul, C.J. Carpenter, J.E. Bushnell, P.A.M. van Koppen, M.T. Bowers, J. Am. Chem. Soc. 120 (1998) 6785.
[37] W.L. Hase, Y.J. Cho, J. Chem. Phys. 98 (1993) 8626.
[38] Y.J. Cho, S.R. VandeLinde, L. Zhu, W.L. Hase, J. Chem. Phys. 96 (1992) 8275.
[39] S.R. VandeLinde, W.L. Hase, J. Chem. Phys. 93 (1990) 7962.
[40] S.R. VandeLinde, W.L. Hase, J. Phys. Chem. 94 (1990) 2778.
[41] K. Kimura, S. Katsumata, Y. Achiba, T. Yamazaki, S. Iwata, Handbook of He I Photoelectron Spectra of Fundamental Organic Molecules, Halsted Press, New York, 1980.